



Publication Year	2015
Acceptance in OA @INAF	2023-02-27T09:57:43Z
Title	C-band observations of supernova remnants with SRT: 2 - Calibrations
Authors	EGRON, Elise Marie Jeanne; PELLIZZONI, ALBERTO PAOLO; IACOLINA, Maria Noemi; LORU, Sara; RIGHINI, SIMONA; et al.
Handle	http://hdl.handle.net/20.500.12386/33879
Number	AV-REP-007



Doc. No.: AV-REP-007

Issue No.: 01

Issue Date: 14/12/15

Title: C-band Observations of Supernova Remnants with SRT:
II - Calibrations

Pages: 14

C-band Observations of Supernova Remnants with SRT: II - Calibrations

	Name	Date
Authors	E. Egron, A. Pellizzoni, M.N. Iacolina, S. Loru, S. Righini, A. Trois et al. on behalf of the Astronomical Validation Team and in collaboration with UNICA student: G. Murtas	14/12/15

DOCUMENT CHANGE RECORD					
Issue No.	Issue date	No. of pages	Pages changed, added, deleted	Description of change	Contacts
01	14/12/15	14	-	Issue 01	egron@oa-cagliari.inaf.it
					apellizz@oa-cagliari.inaf.it
					iacolina@oa-cagliari.inaf.it

Introduction

Following to the Astronomical Validation report n°6 (AV-rep-006; Egron et al. 2015) dedicated to the C-band imaging performances of SRT through the observation of two Supernova Remnants (3C157 and W44), this second note is devoted to the calibration of the resulting maps. It represents the final step of the imaging data analysis procedure with SDI (Single Dish Imager; Pellizzoni et al. in prep), involving the conversion of the “counts maps” into brightness (Jy/sr), in order to reconstruct the integrated flux density of the targets (Jy) and compare it with literature values.

We selected a set of six calibrators, which are strong radio sources well known in literature for their constant flux density on long time scales. They appear as point-like sources for SRT, providing the possibility to perform a few cross-scans to determinate the factor of conversion in Jy/counts. This factor is then applied on the maps to determinate the flux density of the targets.

Long term monitoring of calibrators

We conducted the monitoring of the radio sources 3C147, 3C48, 3C123, NGC7027, 3C295 and 3C286 at different elevations from 27 May 2014 to 11 September 2015, in order to check the stability of the C-band gain curve with the time, and test the consistency of the conversion factors and the associated errors for the different calibrators.

These observations were performed before and after each observation of our targets, W44 and 3C157. Additional calibration observations were carried out a few months later, after the campaign on these SNRs to cover a larger time scale. They consist of two On The Fly (OTF) cross scans of 0.5° each in RA and DEC, at the constant velocity of $4^\circ/\text{min}$. A total of 179 calibration observations were performed, resulting in 708 subscans. For each subscan, SDI performs the automatic subtraction of the baseline, then applies a Gaussian fit to measure the maximum of the counts (proportional to the flux density), and the associated error for both left and right channels.

The spectral flux density of the calibrators at the observed frequency (central frequency 7.2 GHz, LO=6800 MHz, BW=680 MHz) was reconstructed/extrapolated from the values and the polynomial expressions proposed by Perley et al. (2013) using the VLA (see Table 1). 3C123, 3C286 and 3C295 present flux variations of less than 5% per century between 1 and 50 GHz. Of these sources, 3C286 appears as the most suitable calibrator because of the compactness of the source and the flatness of the spectral index. The other sources are found to vary significantly on various timescales (Perley et al. 2013).

Calibrator	3C147	3C48	3C123	NGC7027	3C295	3C286
Flux density (Jy)	5.1885	3.6722	11.0837	5.6107	4.1610	5.7194

Table 1. Flux density of the calibrators at 7.2 GHz (values extrapolated from Perley et al. 2013).

The factor of conversion of the measured counts and spectral flux density was established for each calibrator at the various elevations by performing the average of the values associated to two consecutive cross-scans. A summary table (see Annex I) is automatically generated by SDI and reports the number of the observation, epoch of

observation (MJD), name of the calibrator, elevation, frequency, bandwidth, attenuation of the Total Power, counts, errors, factor of conversion (Jy/counts) of both left and right channels.

We present in Figure 1 the conversion factors for the different calibrators, in chronological order. The values are distributed over four different levels, depending on the signal attenuation selected during the observations to keep the observations in the linear range of the Total Power (to provide a linear conversion between counts and Jy). The weather conditions clearly impact on the attenuation of the signal. For instance, the humidity considerably increased during the observations performed the night of the 23 July 2015, which led us to modify the signal attenuation from 7 to 10 dB (around calibrator id 140 in Fig.1). The associated conversion factor was about 0.06 Jy/counts in the first case, then about 0.13 Jy/counts for 10 dB of attenuation. Note also the values of the calibration factors obtained during the session of the 10 December 2014 with the attenuation set at 8 dB (calibrator id 61), which are the same than those obtained when the attenuation set at 7 dB (possibly related to the initial choice of the raw counts readout (T_{pi}), which has to be within the 750-1000 counts range in any weather conditions to keep the observations in the linear range of the Total Power). This needs further investigations.

The conversion factors present some variations/dispersions of about 0.01 Jy/counts for a given attenuation. However, the conversion factor associated to each calibrator appears in general quite stable over time for a same attenuation, at the exception of 3C48 that shows larger fluctuations. This calibrator is known to be weaker than the other ones. It is worth noting that the values corresponding to NGC7027, 3C147 and 3C48 are usually lower than that of the three other calibrators. Considering the conclusions drawn by Perley et al. (2013), the values from 3C286, 3C295 and 3C123 could be more trusted.

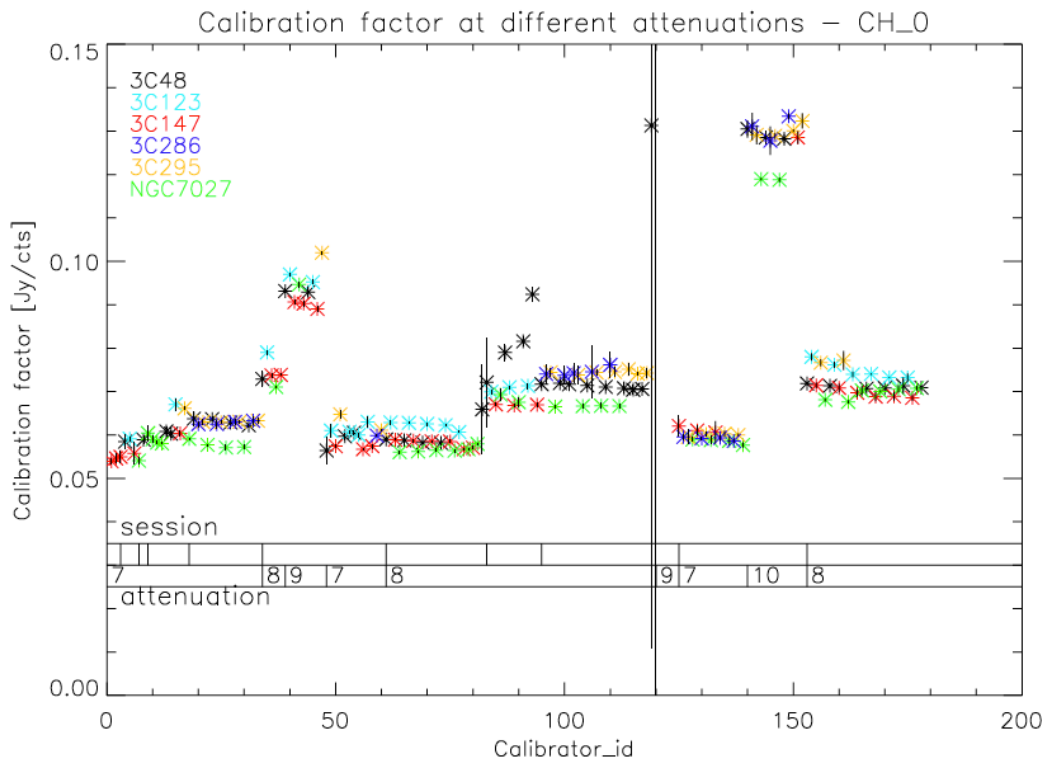


Figure 1: Calibration factor for the different radio sources in chronologic order, for four different attenuations (7, 8, 9 and 10 dB), corresponding to the left channel. In the session line, each

separation indicates a different day of observation (see Annex 1 for the recapitulative table of the observations).

In Figure 2, we plot the calibrator factors in function of the elevation for the different attenuations.

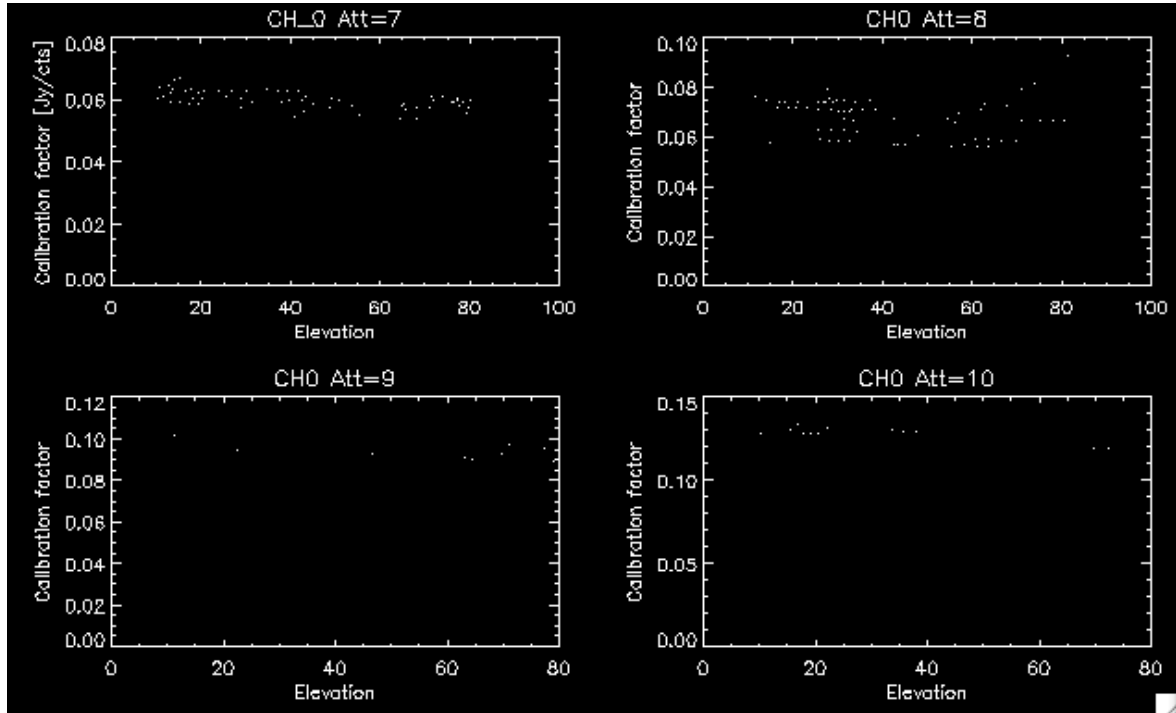


Figure 2: Calibration factor (Jy/counts) in function of the elevation (degrees) considering separately the four attenuations (left channel).

We note a slight trend with a larger conversion factor for lower elevation values. This is most likely due to the small shift in the pointing of antenna, whose effects are stronger at low ($<30^\circ$) and possibly high elevation ($>70^\circ$). It appears necessary to perform a small correction of the pointing model, by adding a correction factor to the Gaussian width of the calibrators, which should be equals to the beam width. Another method consists in using the “calibrationToolClient” to provide the correct offsets for each calibrator at the observed elevations before performing the cross-scans centered on the calibrator. This allows us to reconstruct the “correct” flux at the centered position of the calibrator and thus to optimize the pointing and focusing calibration.

Hence, if 3C286, 3C295 and 3C123 are visible at the moment of the observation of the target, more precise measurements of the calibration should be obtained by excluding the values of the other calibrators. A general strategy consists in performing the average on the different values of the conversion factor obtained at a same attenuation of the target, within an interval of 12 hours to have a correct estimate of the flux density, and to possibly discard the outliers. In this way, the factor/gain stability and related errors can be as low as 1%. Usually, the attenuation is set a 7 dB for good weather and opacity conditions in C-band. Precise correlations among opacity and attenuation are under investigation.

Calibration of maps

The calibration of the maps consists in two steps: the determination of the calibration factor, then the application of the calibration factor to the “counts” map to obtain a calibrated map (in Jy/sr).

In order to provide an accurate value of the factor of conversion, SDI automatically performs the average of the different values associated to the calibrators according to two main criteria:

1) the attenuation set during the observations of the calibrators has to be the same than that of the target to give a correct factor of conversion (Jy/counts).

2) the observations of calibrators are taken in a range of 12 hours from the observation of the target to guarantee the same conditions of observations and the highest stability of the factor of conversion.

Once the calibration factor is calculated, a sub-program of SDI applies this factor to the map of the target to obtain a new calibrated map in Jy/sr. The estimate of the integrated flux of the target is then possible by using the ds9 image of the obtained map and the associated statistical tools, or a sub-program of SDI (mapstat) that directly gives the values of the integrated flux, integrated counts and mean pixel values through the selection of the pixel range. SDI provides integrated flux errors based on an error map taking into account measurement errors for each pixel (this task cannot be performed by ds9).

A) Calibration of SNR 3C157

We proceeded to the calibration of the SNR 3C157 by using first the ds9 image of the target (global map made of 4 observational sessions). We defined the centroid of the diffuse emission, considering a radius of 0.5° to take into account the whole emission from the source, including the faint halos. This method implies a conversion of the emission in Jy/sr (brightness) considering the circular area in arcsec^2 to obtain the integrated flux density in Jy. Since SNRs present a large complexity in the distribution and populations of electrons, it is important to identify the integrated flux density in different regions of the source to better understand the physics of these sources. We estimate the integrated flux in four different areas of the source and the rms associated to the map. The values are listed in Table 2. To facilitate the visualization of these areas, we represented the selected regions in Figure 3. We compared the results obtained with SDI when measuring the average brightness, integrated flux, and the mean pixel value on different pixel ranges (rectangular areas). The statistical error of the mean pixel associated to a region free of the source gives the value of the rms. The results are reported in Table 2. Note that the reported errors on the integrated fluxes correspond only to the statistical errors. Systematic errors on the calibration factors imply higher overall errors on the integrated fluxes (about 1%).

3C157	ds9			SDI (mapstat)	
	centroid	Radius ($^{\circ}$)	Integrated Flux (Jy)	Pixel range (Xmin,Xmax,Ymin,Ymax)	Integrated Flux (Jy)
Source	RA=06:16:57.624 DEC= +22:31:36	0.5 (0.035)*	88.94 (0.43)*	20,120,20,120	89.63 +/- 0.07
Area 1	RA=06:17:54.690 DEC= +22:45:54.64	0.035	1.75	90,100,100,110	4.438 +/- 0.007
Area 2	RA=06:17:39.0 DEC= +22:30:27.92	0.035	0.85	90,100,70,80	2.87 +/- 0.01
Area 3	RA=06:17:13.658 DEC= +22:22:22.18	0.035	1.64	75,85,60,70	4.167 +/- 0.008
Area 4	RA=06:16:49.667 DEC= +22:09:28.20	0.035	0.30	70,80,40,50	0.977 +/- 0.006
Rms (mJy/pixel)	RA=06:14:48.171 DEC= +22:02:31.38	0.19	0.41 mJy/pixel	10,30,10,30	0.51 mJy/pixel

Table 2: Ds9 and mapstat parameters for the estimate of the integrated flux and rms associated to the global map of 3C157. The asterisk (*) indicates the values of the integrated flux scaled to a radius of 0.035° for comparison with the other areas.

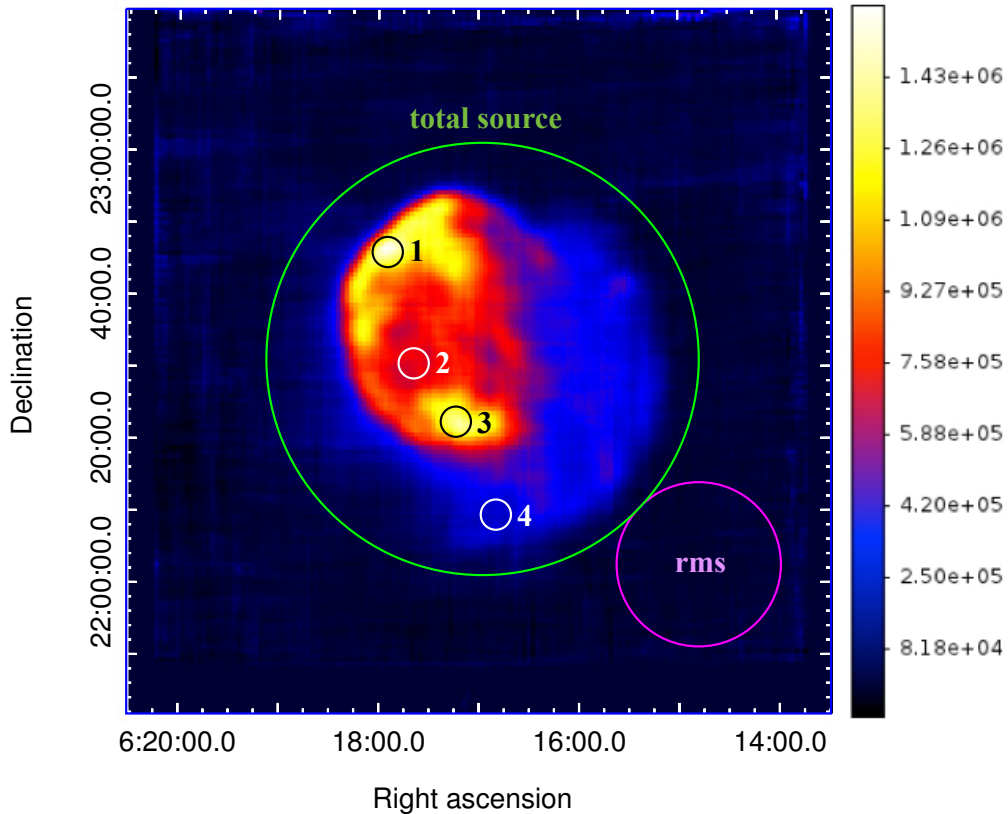


Figure 3: Areas selected for the estimate of the integrated flux in different regions of 3C157 and rms of the map. The values of the flux and parameters of these regions are reported in Table 2. The number indicated in the colored scale represents the brightness in Jy/sr.

The SDI subroutine mapstat and ds9 statistical tools give fully consistent results. The total flux density of 3C157 is estimated at 89.0 ± 0.1 (stat) ± 1 (syst) Jy, with an rms at about 0.5 mJy/pixel. The flux density shows clear variations within the target, indicating very likely different sites of acceleration of various populations of electrons.

In order to estimate separately the integrated flux density from the whole source and the rms associated to the four maps obtained during the different sessions (see AV-rep-006), we applied the same methods than described previously. The values of the integrated flux using the ds9 image of each map were reported on Table 3. The rms was estimated with SDI (statistical error on the mean pixel value of a region free of source).

3C157	27/05/2014	03/06/2014	17/10/2014	10/12/2014	Total
Integrated flux (Jy)	83.33 +/- 0.3	93.16 +/- 0.2	91.27 +/- 0.2	104.9 +/- 0.3	88.94 +/- 0.07
Effective Duration (h)	1h42	1h50	2h46	1h50	8h08
Rms (mJy/pixel)	0.91	0.82	0.57	1.0	0.51
(mJy/beam)	17.8	16.0	11.1	19.5	9.9

Table 3: Comparison of the integrated flux and rms for the individual observations reported in the AV-rep-006, using the same areas than that reported in Table 2. For comparison, we also reported the results of the global map (total).

It is interesting to note the different values associated to the integrated flux density between the four observations due to the presence of RFI that are not correctly removed by the automated SDI procedure (see p.8 AV-rep-006). As expected, the rms and the statistical errors of the integrated flux associated to the global map are much lower than those associated to the individual maps. This implies that for the automated SDI calibration procedure, two/three repeated maps are required. Otherwise, manual RFI removal would be necessary when adopting just one map.

Note that the observations corresponding to the 10 December 2014 present a higher flux density than the other ones. This could be related to the RFI and/or to the unexpected calibration factor associated to the attenuation set at 8 dB.

We compared our results with the literature, in particular with the recent measurements performed at 6cm with Urumqi, the sino-german 25m telescope, which carried out the polarization survey of the Galactic plane with an angular resolution of 9.5'. Gao et al. (2011) reported the integrated flux density and derived the radio spectra of 16 SNRs, including 3C157, by using the flux density at different frequencies obtained with Effelsberg during the 11cm and 21cm surveys. The radio sources 3C286, 3C48 and 3C138 were used for the calibration of the total intensity. The associated flux densities at 6cm are 7.5 Jy, 5.5 Jy and 3.9 Jy, respectively. The large-scale Galactic diffuse emission was filtered by using the technique of "background filtering" (Sofue & Reich 1979). The background was estimated by averaging the intensity in a polygonal area free of structure. The flux density of the SNR was integrated within a ring boundary around the source defined by 3 times the rms. The integrated flux density of 3C157 was estimated at 84.6 +/- 9.4 Jy at 6cm (central frequency 4.8 GHz). The larger errors associated with Urumqi are likely related to the technique of observation, i.e. raster map (3' separation subscans) with the subtraction of the background, instead of OTF map with subtraction of the baseline for SRT, and the larger angular resolution (9.5' instead of 2.6' for SRT in C-band).

The Urumqi observations at 6cm together with other observations made at different wavelength (Reich et al. 2003; Erickson et al. 1985) gave an overall radio spectral index of $\alpha = -0.38 \pm 0.01$. We extrapolated the value to estimate the theoretical flux density at 7.2

GHz; $S_{7.2\text{GHz}} = S_{4.8\text{GHz}} * (v_{7.2\text{GHz}}/v_{4.8\text{GHz}})^{-0.38}$, with $S_{4.8\text{GHz}} = 84.6$ Jy. The theoretical flux density is about 73 ± 8 Jy, which is compatible with the value we obtained with SRT at 2 sigma (89 ± 1 Jy). The results are consistent within two sigma, although differences could be mostly related to actual area selected to measure the flux density (not precisely reported by Gao et al. 2011).

Green et al. (1986) proposed a variation of the spectral indices in the structure of 3C157. This hypothesis was confirmed by Leahy et al. (2004) who found a spectral index of $\alpha = -0.43 \pm 0.02$ in the brightened northwestern shell region whereas the fainter southern part indicates variations in the range $\alpha = -0.2$ to $\alpha = -0.6$.

B) Calibration of SNR W44

We used the same methods than described previously to calibrate the maps of W44. The selection of the area to estimate the integrated flux density is more complex because of the presence of the sources in the vicinity of the SNR, in particular the emission from the non-identified source and from the Galactic plane. We considered circular areas (with ds9) centered on W44 and on the non-identified source, and a rectangular area along the Galactic plane to estimate the different contributions of the flux density. An illustration of these areas is shown in Figure 4, in addition to the region selected for the rms. We then compared the results with mapstat, using rectangular areas to estimate the flux density of W44 and the non-identified source. Note that the area selected for W44 includes the non-identified source and a small contribution of the Galactic plane, which needs to be subtracted to have a correct estimate of the source.

W44	ds9			mapstat	
	centroid	Radius (°)	Integrated Flux (Jy)	Pixel range (Xmin,Xmax,ymin,ymax)	Integrated Flux (Jy)
Source	RA=18:56:05.1 DEC=+01:21:36	0.32	129.51	*37,98,22,86	133.87 +/- 0.06
Non-identified source	RA=18:57:03.41 DEC=+01:38:58.13	0.054	2.03	80,98,77,88	2.11 +/- 0.01
Galactic plane (galactic coord)	+34:38:56.8 +00:00:17.4	**	9.18	n/a	n/a
Rms (mJy/pixel)	RA=18:56:24.85 DEC=+00:57:28.61	0.08	0.60	50,70,2,15	0.62

Table 4: Ds9 and mapstat parameters for the estimate of the integrated flux density and rms associated to the global map of W44. *This region also includes the non-identified source whose flux density has to be subtracted to estimate the flux density from the source and a small contribution from the Galactic plane. **We considered a rectangular box ($0.7^\circ \times 0.2^\circ$) to measure the integrated flux from the Galactic plane.

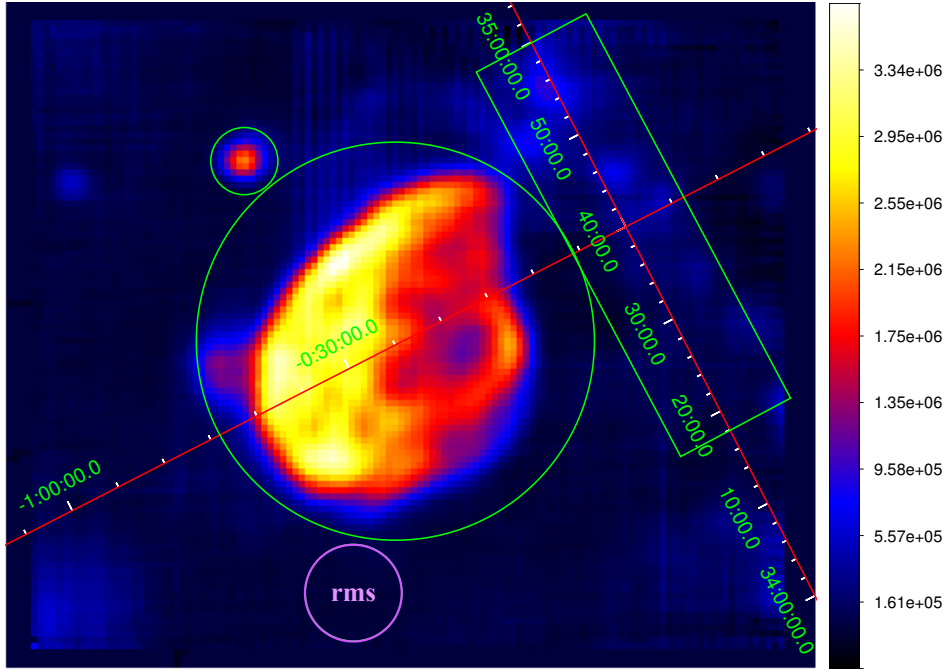


Figure 4: Areas selected with ds9 for the estimate of the integrated flux density and rms in different regions of W44, reported in Table 4. The circle on upper left of the SNR indicates the non-identified source whereas the rectangular box represents the emission from the Galactic plane. Axes are in galactic coordinates.

The total flux density of W44 is estimated at 129.5 ± 0.1 (stat) ± 1.3 (syst) Jy, with an rms at about 0.6 mJy/pixel. The Galactic plane has a contribution of about 9 Jy (considering the area of $0.7^\circ \times 0.2^\circ$), while the non-identified source presents a flux density of about 2 Jy.

We compared the values of the integrated flux density and rms associated to the single maps (corresponding to the three sessions) with those of the global map. The values are extremely similar, as shown in Table 5, with a lower value of the rms in the case of the global map, as expected. Note that some RFI were visible only during the first observational session of W44 performed on 09/07/2014, which explains the higher rms associated to this map. However, the flux density values are extremely similar, in contrast to the observations of 3C157.

W44	09/07/2014	11/09/2014	16/09/2014	Total
Integrated flux (Jy)	130.26	129.10	130.92	129.51
Effective Duration (h)	0h59	0h59	2h56	4h54
Rms (mJy/pixel)	1.7	0.82	0.72	0.62
(mJy/beam)	33.2	16.0	14.0	12.1

Table 5: Comparison of the integrated flux and rms for the individual observations of W44 reported in the AV-rep-006, using the same areas (with ds9) than that reported in Table 4. For comparison, we also reported the results of the global map (total).

The integrated flux density of W44 obtained with SRT at 7.2 GHz is about 129.5 ± 1.3 Jy. For comparison, the measurements performed by Urumqi at 6cm gave an

estimate of 118 ± 6 Jy (Sun et al. 2011). A previous estimate at 127 ± 13 Jy was made at 5.0 GHz (Altenhoff et al. 1970), during the survey of the Galactic plane carried out with the Green Bank telescope (half-power beam width $10.8'$). The differences in these values are most likely related to the methods used for the subtraction of the background in such a complex environment, in particular due to the emission from the Galactic plane in the vicinity of W44. The subtraction of the baseline appears as the most reliable method since it is a direct and precise subtraction of the real background and not an estimate as in the case of Urumqi.

Sun et al. (2011) reported a spectral index of $\alpha = -0.37 \pm 0.02$ in the case of W44. We extrapolated the values at 5 GHz indicated by Sun et al. (2011) and Altenhoff et al. (1970) to estimate the theoretical flux density at 7.2 GHz and compare it with the value obtained with SRT. The expected flux densities at 7.2 GHz are about 102 ± 5 Jy and 111 ± 11 Jy, respectively. These values are compatible at 5 sigma and 2 sigma, respectively, with that of SRT (129.5 ± 1.3 Jy).

Note that some sources cannot be separated from the SNR, which implies an additional difficulty and imprecision in the determination of the flux density of the target. It is the case of the strong thermal emission located in $ra=18h56m47.9s$, $dec=01^{\circ}17'54''$ (named G034.7-00.6; Paladini et al. 2003), which is a young stellar object located on the border of W44.

Summary and Open issues

We performed the calibration of the SNR 3C157 and W44, observed with the SRT in C-band using the Total Power backend. The monitoring of six calibrators demonstrated a quite stable count-to-flux conversion over one year. However, a slight trend (0.01 Jy/counts) is present providing a larger conversion factor for lower elevation values, probably related to the small shift in the pointing of antenna and not related to the gain.

The implementation of a time and attenuation filter in the Single Dish Imager software enables the automated selection of calibration sources observed within 12 hours of the target to better take into account of the overall observation conditions. We checked the consistency of the integrated flux values obtained with the most refined SDI baseline subtraction method (time consuming) and with the less complex methods (quicklook) providing different accuracy. The integrated flux densities obtained with the SRT calibrated maps of SNR 3C157 and W44 are in agreement with the literature, with smaller error bars mostly due to our “map oversampling” technique. In our method, statistical errors can be precisely assessed and they result much lower (typically about 0.1%) than systematics due to calibration errors (1%). When running the automated version of SDI, the mapping of the target should be repeated 2-3 times in order to properly identify and remove the RFI without manual intervention (too time consuming and then unfeasible when using multi-feed multi-channel spectro-polarimetric backends) and to guarantee $<10\%$ systematic errors.

This testifies the robustness of the SDI (including the methods used for the automated subtraction of the baseline, RFI identification, calibration) and the capacity of SRT in mapping extended sources using the OTF observations.

Moreover, the SDI software offers the possibility to estimate the flux density in different regions of the SNRs with a great precision. This will allow us to better understand the complex morphology of such sources, and to possibly identify different sites of

accelerations of the various populations of electrons within the source. The next step will be the implementation of spectral imaging in SDI.

References

- Altenhoff W.J., Downes D., Pauls T. and Schraml J. 1979, A&AS, 35, 23
 Egron E., Pellizzoni A., Iacolina N. et al. 2015, Internal Report AV-REP-006
 Erickson W.C. & Mahoney M.J. 1985, ApJ, 290, 596
 Gao X.Y., Han J.L., Reich W. et al. 2011, A&A, 5291, A159
 Paladini R., Burigana, C., Davies, R. D. et al. 2003, A&A, 397, 213
 Perley R.A. & Butler B.J. 2013, ApJS, 204, 19
 Reich W., Zhang X. and Furst E. 2003, A&A, 408, 961
 Sofue & Reich 1979, A&AS, 38, 251
 Sun X. H., Reich P., Reich W. et al. 2011, A&A, 536, A83

Annex

Extract of the summary reporting calibrators observed with SRT in C-band with the Total Power from 27 May 2014 to 11 September 2015.

Two cross-scans were performed for each calibrator. We reported the number of the observation, MJD, name of the calibrator, elevation (°), LO (MHz), observed BW (MHz), attenuation of the left channel (“L”), attenuation of the right channel (“R”), baseline subtracted counts (L), error on the counts (L), baseline subtracted counts (R), error on the counts (R), calibration factor (L) in Jy/counts obtained as the ratio of the calibrator flux over the measured counts, error on the calibration factor (L), calibration factor (R), error on the calibration factor (R).

Then, for each set of two cross-scans associated to the calibrators, we reported the calibration number (CAL), MJD, calibrator name, elevation (°), LO (MHz), BW (MHz), attenuation (L), attenuation (R), average of the counts related to the four observations (L), error on the counts (L), average of the counts related to the four observations (R), error on the counts (R), average of the calibration factor (L), error on the average of the calibration factor (L), average of the calibration factor (R), error on the average of the calibration factor (R).

In the following, we reported the information related to some calibrator observations performed on 27 May, 3 June, 9 July, 10 December 2014 and 4 June 2015.

1	56804.6078	3C147	68.2	6900	680	7	7	95.63	0.27	101.22	0.28	0.0543	0.0513
2	56804.6080	3C147	68.2	6900	680	7	7	97.51	0.34	104.58	0.33	0.0532	0.0496
3	56804.6082	3C147	68.1	6900	680	7	7	96.51	0.23	104.22	0.24	0.0538	0.0498
4	56804.6084	3C147	68.1	6900	680	7	7	96.79	0.27	104.82	0.31	0.0536	0.0495

CAL1	56804.6084	3C147	68.1	6900	680	7	7	96.21	1.05	103.64	1.59	0.05393	0.05006	0.00059	0.00077
------	------------	-------	------	------	-----	---	---	-------	------	--------	------	---------	---------	---------	---------

5	56804.7252	3C147	41.3	6900	680	7	7	94.73	0.33	102.22	0.36	0.0548	0.0508
---	------------	-------	------	------	-----	---	---	-------	------	--------	------	--------	--------

6	56804.7254	3C147	41.2	6900	680	7	7	94.77	0.30	101.92	0.31	0.0547	0.0509		
7	56804.7256	3C147	41.2	6900	680	7	7	96.59	0.41	104.71	0.26	0.0537	0.0496		
8	56804.7258	3C147	41.1	6900	680	7	7	97.14	0.44	105.42	0.25	0.0534	0.0492		

CAL2	56804.7258	3C147	41.1	6900	680	7	7	94.98	1.77	102.23	2.76	0.05463	0.05075	0.00102	0.00137

9	56811.3809	3C147	55.1	6900	680	7	7	92.44	0.32	98.36	0.32	0.0561	0.0528		
10	56811.3811	3C147	55.2	6900	680	7	7	92.17	0.28	97.47	0.29	0.0563	0.0532		
11	56811.3813	3C147	55.3	6900	680	7	7	95.02	0.24	102.48	0.25	0.0546	0.0506		
12	56811.3816	3C147	55.3	6900	680	7	7	95.15	0.26	102.67	0.24	0.0545	0.0505		

CAL3	56811.3816	3C147	55.3	6900	680	7	7	94.39	2.08	101.28	3.30	0.05497	0.05123	0.00121	0.00167

13	56811.4982	3C48	45.3	6900	680	7	7	60.68	0.17	64.91	0.19	0.0605	0.0566		
14	56811.4984	3C48	45.3	6900	680	7	7	62.87	0.22	67.43	0.21	0.0584	0.0545		
15	56811.4986	3C48	45.2	6900	680	7	7	62.94	0.16	67.50	0.17	0.0583	0.0544		
16	56811.4988	3C48	45.2	6900	680	7	7	64.76	0.22	69.07	0.23	0.0567	0.0532		

CAL4	56811.4988	3C48	45.2	6900	680	7	7	62.81	1.67	67.23	1.72	0.05846	0.05462	0.00156	0.00140

17	56811.5015	3C123	76.0	6900	680	7	7	187.36	0.55	202.94	0.69	0.0592	0.0546		
18	56811.5017	3C123	76.0	6900	680	7	7	188.89	0.59	203.37	0.67	0.0587	0.0545		
19	56811.5019	3C123	75.9	6900	680	7	7	185.64	0.62	200.71	0.58	0.0597	0.0552		
20	56811.5021	3C123	75.9	6900	680	7	7	187.74	0.59	198.64	0.75	0.0590	0.0558		

CAL5	56811.5021	3C123	75.9	6900	680	7	7	187.41	1.34	201.41	2.19	0.05914	0.05503	0.00042	0.00060

236	57001.7229	3C48	60.7	6900	680	8	8	61.89	0.16	68.02	0.15	0.0593	0.0540		
237	57001.7231	3C48	60.8	6900	680	8	8	62.02	0.21	68.40	0.21	0.0592	0.0537		
238	57001.7233	3C48	60.8	6900	680	8	8	62.52	0.17	69.34	0.19	0.0587	0.0530		
239	57001.7235	3C48	60.9	6900	680	8	8	62.77	0.18	69.88	0.18	0.0585	0.0525		

CAL61	57001.7235	3C48	60.9	6900	680	8	8	62.30	0.42	68.91	0.85	0.05894	0.05329	0.00039	0.00066

240	57001.7251	3C123	25.7	6900	680	8	8	175.66	0.48	192.89	0.53	0.0631	0.0575		
241	57001.7253	3C123	25.7	6900	680	8	8	175.14	0.49	192.43	0.54	0.0633	0.0576		
242	57001.7255	3C123	25.8	6900	680	8	8	177.11	0.42	196.75	0.47	0.0626	0.0563		
243	57001.7257	3C123	25.8	6900	680	8	8	177.31	0.53	197.33	0.56	0.0625	0.0562		

CAL62	57001.7257	3C123	25.8	6900	680	8	8	176.30	1.07	194.85	2.55	0.06287	0.05688	0.00038	0.00074

244	57001.7265	3C147	25.8	6900	680	8	8	88.22	0.30	97.11	0.32	0.0588	0.0534		
245	57001.7267	3C147	25.9	6900	680	8	8	88.03	0.24	96.42	0.25	0.0589	0.0538		
246	57001.7270	3C147	26.0	6900	680	8	8	88.24	0.27	98.16	0.25	0.0588	0.0529		
247	57001.7272	3C147	26.0	6900	680	8	8	87.77	0.26	97.90	0.29	0.0591	0.0530		

CAL63	57001.7272	3C147	26.0	6900	680	8	8	88.06	0.22	97.40	0.79	0.05892	0.05327	0.00015	0.00043

248	57001.7300	NGC7027	63.9	6900	680	8	8	100.27	0.30	110.57	0.29	0.0560	0.0507		
249	57001.7302	NGC7027	63.9	6900	680	8	8	100.61	0.38	111.47	0.37	0.0558	0.0503		
250	57001.7304	NGC7027	63.8	6900	680	8	8	100.01	0.26	110.95	0.27	0.0561	0.0506		
251	57001.7306	NGC7027	63.8	6900	680	8	8	99.58	0.27	110.73	0.29	0.0563	0.0507		

CAL64	57001.7306	NGC7027	63.8	6900	680	8	8	100.12	0.44	110.93	0.39	0.05604	0.05058	0.00024	0.00018

252	57001.7333	3C48	63.6	6900	680	8	8	61.81	0.18	68.59	0.21	0.0594	0.0535		
253	57001.7335	3C48	63.7	6900	680	8	8	62.51	0.17	68.95	0.17	0.0587	0.0533		
254	57001.7337	3C48	63.8	6900	680	8	8	62.61	0.20	69.45	0.23	0.0587	0.0529		
255	57001.7339	3C48	63.8	6900	680	8	8	63.00	0.18	70.19	0.18	0.0583	0.0523		

CAL65	57001.7339	3C48	63.8	6900	680	8	8	62.48	0.50	69.29	0.69	0.05877	0.05299	0.00047	0.00053

256	57001.7352	3C123	28.3	6900	680	8	8	176.33	0.59	193.75	0.62	0.0629	0.0572		
257	57001.7354	3C123	28.4	6900	680	8	8	176.76	0.45	194.11	0.49	0.0627	0.0571		
258	57001.7356	3C123	28.5	6900	680	8	8	176.53	0.45	195.63	0.49	0.0628	0.0567		
259	57001.7358	3C123	28.5	6900	680	8	8	176.28	0.53	195.98	0.58	0.0629	0.0566		

CAL66 57001.7358 3C123 28.5 6900 680 8 8 176.48 0.22 194.87 1.10 0.06281 0.05688 0.00008 0.00032

324 57177.2676 3C48 67.7 6900 680 8 8 47.41 0.24 55.51 0.28 0.0775 0.0661
325 57177.2678 3C48 67.8 6900 680 8 8 47.74 0.32 55.95 0.39 0.0769 0.0656
326 57177.2680 3C48 67.9 6900 680 8 8 47.84 0.21 55.89 0.22 0.0768 0.0657
327 57177.2682 3C48 67.9 6900 680 8 8 47.82 0.20 55.77 0.21 0.0768 0.0658

CAL83 57177.2682 3C48 67.9 6900 680 8 8 50.92 7.19 58.95 7.09 0.07212 0.06229 0.01018 0.00749

328 57177.2699 3C123 32.4 6900 680 8 8 157.62 0.50 181.24 0.56 0.0703 0.0612
329 57177.2701 3C123 32.5 6900 680 8 8 157.98 0.43 182.11 0.49 0.0702 0.0609
330 57177.2703 3C123 32.6 6900 680 8 8 159.57 0.57 184.53 0.54 0.0695 0.0601
331 57177.2705 3C123 32.6 6900 680 8 8 158.62 0.50 183.53 0.53 0.0699 0.0604

CAL84 57177.2705 3C123 32.6 6900 680 8 8 158.45 0.85 182.85 1.46 0.06995 0.06062 0.00038 0.00049

332 57177.2719 3C147 31.1 6900 680 8 8 77.31 0.22 89.70 0.28 0.0671 0.0578
333 57177.2720 3C147 31.2 6900 680 8 8 77.89 0.21 89.72 0.24 0.0666 0.0578
334 57177.2723 3C147 31.3 6900 680 8 8 77.25 0.25 90.14 0.27 0.0672 0.0576
335 57177.2725 3C147 31.2 6900 680 8 8 77.14 0.23 90.50 0.26 0.0673 0.0573

CAL85 57177.2725 3C147 31.2 6900 680 8 8 77.40 0.34 90.01 0.38 0.06704 0.05764 0.00029 0.00024

336 57177.2750 NGC7027 57.2 6900 680 8 8 82.96 1.06 94.69 1.04 0.0676 0.0593
337 57177.2752 NGC7027 57.1 6900 680 8 8 81.65 1.65 92.26 0.94 0.0687 0.0608
338 57177.2754 NGC7027 57.0 6900 680 8 8 79.93 0.74 94.04 0.64 0.0702 0.0597
339 57177.2756 NGC7027 57.1 6900 680 8 8 79.43 1.06 94.10 1.23 0.0706 0.0596

CAL86 57177.2756 NGC7027 57.1 6900 680 8 8 80.99 1.62 93.77 1.05 0.06928 0.05983 0.00139 0.00067

340 57177.2787 3C48 70.8 6900 680 8 8 45.92 0.32 54.30 0.34 0.0800 0.0676
341 57177.2789 3C48 70.9 6900 680 8 8 45.27 0.37 53.74 0.40 0.0811 0.0683
342 57177.2791 3C48 70.9 6900 680 8 8 47.60 0.20 54.72 0.26 0.0771 0.0671
343 57177.2793 3C48 70.9 6900 680 8 8 47.18 0.25 54.24 0.26 0.0778 0.0677

CAL87 57177.2793 3C48 70.9 6900 680 8 8 46.49 1.09 54.25 0.41 0.07899 0.06769 0.00185 0.00051
